Non-repeatability effects on time-lapse elastic full-waveform inversion for VSP seismic data

Xin Fu, Kris Innanen, Scott Keating, Qi Hu

ABSTRACT

In this study, we investigate non-repeatability effects on time-lapse elastic full-waveform inversion for VSP (vertical seismic profile) seismic data. The non-repeatabilities tested are the non-repeatability on source locations, the non-repeatability on random noises, and the non-repeatability on the near-surface properties. Four time-lapse inversion strategies, including the parallel strategy, the sequential strategy, the double-difference strategy, and the common-model strategy, are applied in each type of non-repeatability. From the investigation, we can conclude: P-wave velocity changes can be better recovered than S-wave velocity changes; except for the double-difference strategy, the other three strategies have similar performance; the double-difference strategy also has similar performance to the others when acquisition geometries for baseline and monitor surveys are identical, but it is sensitive to the non-repeatability on source locations between twice surveys; no strategies can effectively handle the case of random noise; near-surface property changes have limit impact on the recovery of time-lapse changes for VSP data.

INTRODUCTION

Applying time-lapse (4D) seismic methods for reservoir monitoring and characterization has developed for a long time since the mid-late 1980s (Greaves and Fulp, 1987; Lumley, 2001; Landrø, 2001; Calvert, 2005; Hicks et al., 2016; Jack, 2017; Cho and Jun, 2021), which can be employed to monitor reservoir changes caused by the production of hydrocarbon (e.g., enhanced oil recovery) and the unground storage of CO_2. Especially, due to the increasing demand for technologies to control greenhouse gas emissions, storing CO_2 in the subsurface has been being developing by many researchers, and 4D seismic methods are used to monitor the CO_2 storages accordingly (Egorov et al., 2017; Cho and Jun, 2021; Ajo-Franklin et al., 2013; Macquet et al., 2019). However, successful seismic monitoring depends on the repeatability between baseline and monitor surveys that can be affected by variations in weather conditions, source and receiver positions, environmental noises, source wavelets, seawater or near-surface properties, etc.

The impact of the variations can be alleviated by good acquisition plans and/or proper processing, e.g., repeatable acquisition geometries and data processing procedures. To obtain good repeatable data to monitor the reservoir changes, the permanent OBC (ocean-bottom-cable) installations are set at Foinhaven and Valhall fields (Calvert, 2005; Yang et al., 2016). And at the Aneth oil field in Utah, the receivers are cemented in the monitor well to acquire time-lapse VSP (vertical seismic profile) data (Cheng et al., 2010). In the CO2CRC Otway field experiment, Shulakova et al. (2015) improve the repeatability of the land seismic data by burying the receivers which can lower the noises caused by poor weather conditions, non-repeatable receiver positions, near-surface changes, and non-repeatable survey environments. During the data processing, a cross-equalization method is often applied to enhance the repeatability between baseline and monitor data (Rickett and Lumley, 2001). Fu et al. (2020) propose a double-wavelet method to eliminate the source wavelet non-repeatability which can also be reduced by designing a matching filter (Fu and Innanen, 2022c). In past years, time-lapse seismic surveys based on a fiber-optic distributed acoustic sensing (DAS) system becomes increasingly popular, since the down-hole DAS array can be permanently installed, has lower monitoring cost, and is of finer spatial sampling (Zwartjes et al., 2018; Byerley et al., 2018; Wilson et al., 2021).

As a powerful tool for 4D seismic data inversion to monitor subsurface reservoir changes and/or CO_2 storages, full waveform inversion (FWI) (Lailly et al., 1983; Tarantola, 1984; Virieux and Operto, 2009) has the ability of high-resolution imaging of physical properties for subsurface media, and it can solve the problem of non-repeatable receiver/source positions in time-lapse seismic surveys (Zhou and Lumley, 2021b). In the past decade, many time-lapse FWI methods have been developed. The most conventional time-lapse FWI strategy is the parallel strategy (Lumley et al., 2003; Plessix et al., 2010), but its result is prone to be affected by the convergence difference (Yang et al., 2015) and non-repeatable receiver/source positions (Zhou and Lumley, 2021b; Fu and Innanen, 2022a) between baseline and monitor inversion. Routh et al. (2012) present the sequential strategy, using the inverted baseline model as a starting model for monitor inversion, which can help to save computational cost and has been justified in a field VSP data case (Egorov et al., 2017). However, this strategy often generates strong artifacts since it enhances the convergence difference between twice FWIes (Yang et al., 2015; Zhou and Lumley, 2021b). But a local-updating sequential strategy can efficiently reduce the artifacts and perform well in both synthetic and field time-lapse data (Raknes and Arntsen, 2014; Asnaashari et al., 2015). Also, the local-updating method can be incorporated with the double-difference strategy, which will be introduced later, to improve the time-lapse results (Zhang and Huang, 2013; Li et al., 2021), alleviate the impact of taking an acoustic approximation to elastic subsurface rocks (Willemsen et al., 2016), or implement Bayesian/Markov Chain Monte Carlo formulation of time-lapse FWI (Fu and Innanen, 2022b). And the local-solver-based local-updating method can significantly decrease the computational cost of time-lapse FWI (Willemsen, 2017; Huang et al., 2018; Kotsi et al., 2020). Of course, the local-updating method needs prior location information about reservoir change, which may be difficult to be obtained in some cases of non-repeatable time-lapse surveys, such as the ones in this study.

The double-difference strategy, directly minimizing residuals between synthetic difference data (synthetic monitor data minus synthetic baseline data) and observed difference data (observed monitor data minus observed baseline data), applied in 4D FWI first by Zheng et al. (2011), has been adopted by several researchers (Zhang and Huang, 2013; Raknes and Arntsen, 2014; Yang et al., 2015; Willemsen et al., 2016; Fu and Innanen, 2021) including a real data case in Yang et al. (2016). It can focus on reservoir changes and reduce artifacts outside the reservoir, hence, its result is not sensitive to the convergence degree of the inverted baseline model. Nevertheless, the double-difference strategy requires well repeated time-lapse surveys. Fu et al. (2020) introduce a double-wavelet method to handle the case of non-repeatable baseline and monitor source wavelets. But the double-difference strategy is still vulnerable to the non-repeatability of receiver/source positions. The common-model strategy, presented by Hicks et al. (2016), can also decay the artifacts caused by the divergence difference between baseline and monitor inversions (Fu and Innanen, 2022a). Its philosophy is employing the same relatively well-converged starting model for baseline and monitor FWIes to guide them into the same local minimum, and it has been applied in field cases in Hicks et al. (2016) and Bortoni et al. (2021). Moreover, Maharramov et al. (2016) present a joint method in which baseline and monitor models are simultaneously inverted; Zhou and Lumley (2021a) propose a central-difference strategy containing two sequential strategies; and Fu and Innanen (2022a) build a stepsize-sharing strategy by sharing stepsizes between baseline and monitor inversions, which can eliminate the artifacts linked to the convergence difference and is suitable when the starting model is biased.

In this paper, we will investigate non-repeatability effects on time-lapse elastic full-waveform inversion for VSP seismic data. The non-repeatabilities tested will be the non-repeatability on source locations, the non-repeatability on random noises, and the non-repeatability on the near-surface properties. Four time-lapse inversion strategies, including the parallel strategy (PRS), the sequential strategy (SQS), the double-difference strategy (DDS), and the common-model strategy (CMS), will be applied in each type of non-repeatability.

THEORY

Elastic full-waveform inversion

EFWI Tarantola (1986) starts from a given model $\mathbf{m}_0$ and uses an optimization method to search a model $\mathbf{m}$ that makes the synthetic data $\mathbf{d}_{syn}(\mathbf{m})$ match the observed data $\mathbf{d}_{obs}$ best. Usually, this is achieved by minimizing the L2 norm of data residual $\Delta\mathbf{d}$ ($\mathbf{d}_{syn}(\mathbf{m}) - \mathbf{d}_{obs}$) given by

$$E(\mathbf{m}) = \frac{1}{2}\Delta\mathbf{d}^T\Delta\mathbf{d}^*, \tag{1}$$

where T denotes the transpose of a matrix and $*$ denotes the complex conjugate. For EFWI, the model $\mathbf{m}$ in equation 1 represents the elastic parameters (e.g. P-wave velocity, S-wave velocity, and density), and $\mathbf{d}_{syn}$ is the wave field at receiver positions. In this paper, the wave field is obtained by soveling a frequency-domain 2D elastic wave equation given by

$$\begin{aligned}
&\omega^2\rho u + \frac{\partial}{\partial x}\left[(\lambda+2\mu)\frac{\partial u}{\partial x} + \lambda\frac{\partial v}{\partial z}\right] + \frac{\partial}{\partial z}\left[\mu\left(\frac{\partial u}{\partial z} + \frac{\partial v}{\partial x}\right)\right] + f = 0,\\
&\omega^2\rho v + \frac{\partial}{\partial z}\left[(\lambda+2\mu)\frac{\partial v}{\partial z} + \lambda\frac{\partial u}{\partial x}\right] + \frac{\partial}{\partial x}\left[\mu\left(\frac{\partial u}{\partial z} + \frac{\partial v}{\partial x}\right)\right] + g = 0,\\
&\mu = \rho {V_s}^2,\\
&\lambda = {V_p}^2\rho - 2\mu,
\end{aligned} \tag{2}$$

where ω is the angular frequency; $u = u(x,z,\omega)$, $v = v(x,z,\omega)$, $f = f(x,z,\omega)$, and $g = g(x,z,\omega)$ are, respectively, the horizontal displacement field, the vertical displacement field, the horizontal component of source, and the vertical component of source, all depend on the position (x,z) and ω; λ and μ are Lamé constants; $V_p = V_p(x,z)$, $V_s = V_s(x,z)$, and $\rho = \rho(x,z)$ are, respectively, P-wave velocity, S-wave velocity, and density, all depend on the position. Equation 2 can be discretized and solved by the finite-difference method

(Pratt, 1990) under which it can be formulated as

$$\mathbf{A}\mathbf{u} = \mathbf{s}, \tag{3}$$

where $\mathbf{A}$ is the impedance matrix, $\mathbf{u} = [u, v]^T$ is the displacement vector, and $\mathbf{s} = [f, g]^T$ is the source vector.

The gradient of $E(\mathbf{m})$ in equation 1 with respect to $\mathbf{m}$ can be expressed as

$$\bigtriangledown_{\mathbf{m}} E = -\Re\left\{\left[\frac{\partial \mathbf{u}}{\partial \mathbf{m}}\right]^T \Delta\mathbf{d}^*\right\}, \tag{4}$$

where $\Re$ denotes the real part operator. Differentiating equation 3 with respect to $\mathbf{m}$ gives

$$\mathbf{A}\frac{\partial \mathbf{u}}{\partial \mathbf{m}} = -\frac{\partial \mathbf{A}}{\partial \mathbf{m}}\mathbf{u}, \tag{5}$$

which tells us that the partial derivative wavefield $\partial\mathbf{u}/\partial\mathbf{m}$ can be calculated by solving the wave equation with a virtual source $-\left(\partial\mathbf{A}/\partial\mathbf{m}\right)\mathbf{u}$. Putting equation 5 into equation 4, we have

$$\bigtriangledown_{\mathbf{m}} E = \Re\left\{\mathbf{u}^T\left[\frac{\partial \mathbf{A}}{\partial \mathbf{m}}\right]\mathbf{A}^{-1}\Delta\mathbf{d}^*\right\}, \tag{6}$$

from which, we can see that the adjoint wavefield $\mathbf{A}^{-1}\Delta\mathbf{d}^*$ is obtained by solving the wave equation with the source of the conjugate data residual. $\partial\mathbf{A}/\partial\mathbf{m}$ is referred to the radiation that can be used to investigate the crosstalk situation between different parameters (Brossier et al., 2009).

By minimizing the second-order Taylor expansion of the objective function, we can obtain the equation satisfied by the update of the Newton method, which is given by

$$\mathbf{H}\delta\mathbf{m} = -\bigtriangledown_{\mathbf{m}} E, \tag{7}$$

where $\mathbf{H}$ is the Hessian matrix, the second-order derivative of the misfit $E(\mathbf{m})$ with respect to $\mathbf{m}$. The Hessian matrix can compensate for the sphere spreading energy loss and mitigate the parameter crosstalk. However, the explicit Hessian and its inverse matrix consume huge computation and computer memory, it is unrealistic to find the exact Newton update in large-scale FWI. The truncated Gauss-Newton optimization method can overcome this difficulty. It uses a linear optimization method (the L-BFGS method in this work) to solve equation 7 to obtain a relatively accurate approximate Newton update, and the linear optimation method as a whole only needs to use the product of Hessian matrix and a known vector. After using the truncated Gauss-Newton optimation method, the updated model $\mathbf{m}$ is given by

$$\mathbf{m} = \mathbf{m} + \alpha\delta\mathbf{m}, \tag{8}$$

where α is the step length.

Tested time-lapse inversion strategies

In the introduction section, we have introduced the parallel strategy, the sequential strategy, the double-difference strategy, the common-model strategy, the central-difference strategy, the stepsize-sharing strategy, and the joint method. Exhaustively testing all the methods is too resource-intensive. Hence, in this study, we only test the three typical strategies (the parallel strategy, the sequential strategy, and the double-difference strategy), and the common-model strategy that has been applied in a case with minor seawater velocity changes in Hicks et al. (2016).

Parallel strategy

As the most conventional time-lapse inversion strategy, the parallel strategy, , with workflow illustrated in Figure 1a, includes two independent FWI processes. One is for baseline model inversion, and inputs are the baseline data and a starting model. Another one is for monitor model inversion, and inputs are the monitor data and the same starting model as that in the baseline model inversion. Then the inverted time-lapse model is the inverted monitor model subtract the inverted baseline model. Since FWI is highly non-linear and is easy to be stuck in different minima, the two FWI processes mentioned above often have different convergences and yield many artifacts on the final time-lapse inversion.

Sequential strategy

The sequential strategy, with workflow illustrated in Figure 1b, has the same baseline model inversion as the PRS, using baseline data and a starting model to obtain the baseline model. But the second time inversion, monitor model inversion, is different, in which the inverted baseline model is sequentially employed as the starting model for the monitor model inversion. Then the inverted monitor model minus the inverted baseline model is the time-lapse model.

Double-difference strategy

The double-difference strategy, with workflow illustrated in Figure 1c, also contains twice FWI processes. This first one is still the baseline model inversion, the same as that in the parallel strategy or sequential strategy. In the second monitor model inversion, the starting model is the inverted baseline model, same as the sequential strategy, but the input monitor data are not the observed monitor data which are altered to the composited data:

$$\mathbf{d}_{DD} = \mathbf{F}(\mathbf{m}_{bas}) + (\mathbf{d}_{mon} - \mathbf{d}_{bas}), \tag{9}$$

where $\mathbf{F}(\mathbf{m}_{bas})$ is the synthetic data of inverted baseline model $\mathbf{m}_{bas}$, $(\mathbf{d}_{mon} - \mathbf{d}_{bas})$ is the difference data (observed monitor data $\mathbf{d}_{mon}$ subtract observed baseline data $\mathbf{d}_{bas}$). Accordingly, the misfit function for monitor model inversion becomes:

$$\mathbf{E}_{DD}(\mathbf{m}_{mon}) = \frac{1}{2}||\mathbf{d}_{DD} - \mathbf{F}(\mathbf{m}_{mon})||_2^2, \tag{10}$$

where $\mathbf{F}(\mathbf{m}_{mon})$ is the synthetic data of inverted monitor model $\mathbf{m}_{mon}$.

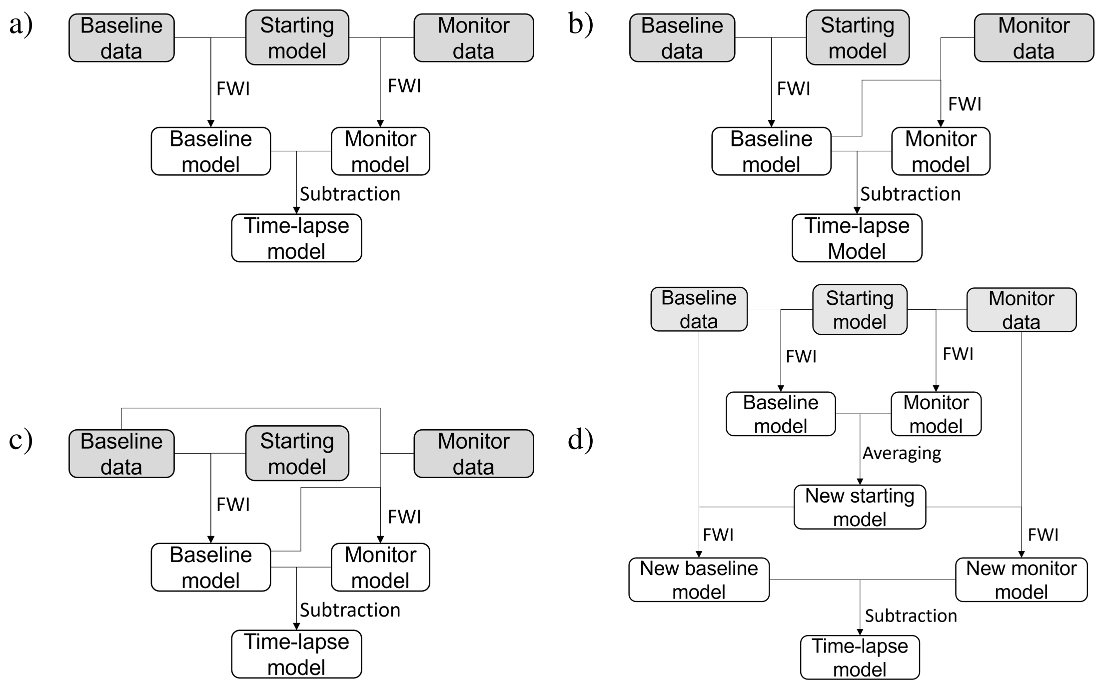

FIG. 1. Workflows of (a) the parallel strategy (PRS), (b) the sequential strategy (SQS), (c) the double-difference strategy (DDS), and (d) the common-model strategy (CMS).

Common-model strategy

The common-model strategy, with workflow illustrated in Figure 1d, can be seen as an upgraded version of the strategy. Essentially, it contains twice parallel strategies. Firstly, the baseline and monitor model inversions are performed independently with the same starting model. Then a new starting model is taken from the average of baseline and monitor models, with which the baseline and monitor model inversions are performed independently again, still using the original data sets. And the final time-lapse change is obtained from the difference of baseline and monitor models in the second-time parallel strategy.

Note that in the original version of the common-model strategy in Hicks et al. (2016), the first-time parallel strategy only uses low-frequency seismic components, and only high-frequency seismic components are employed in the second-time parallel strategy. It may cause a low-frequency component lack in the final inverted time-lapse change. Hence, we use all-frequency seismic components for every single FWI process to enhance the original version.

NUMERICAL TESTS

An elastic time-lapse model is employed to investigate the non-repeatability effects Non-repeatability effects on time-lapse elastic full-waveform inversion for VSP seismic data. The model is plotted in Figure 2a-f including a baseline model and a monitor model. And the time-lapse changes for P- and S- velocities, and density are plotted in Figure 2g-i. The acquisition geometries for baseline and monitor surveys are, respectively, plotted in 2a and d, which are identical at the beginning. The red stars and dash lines represent

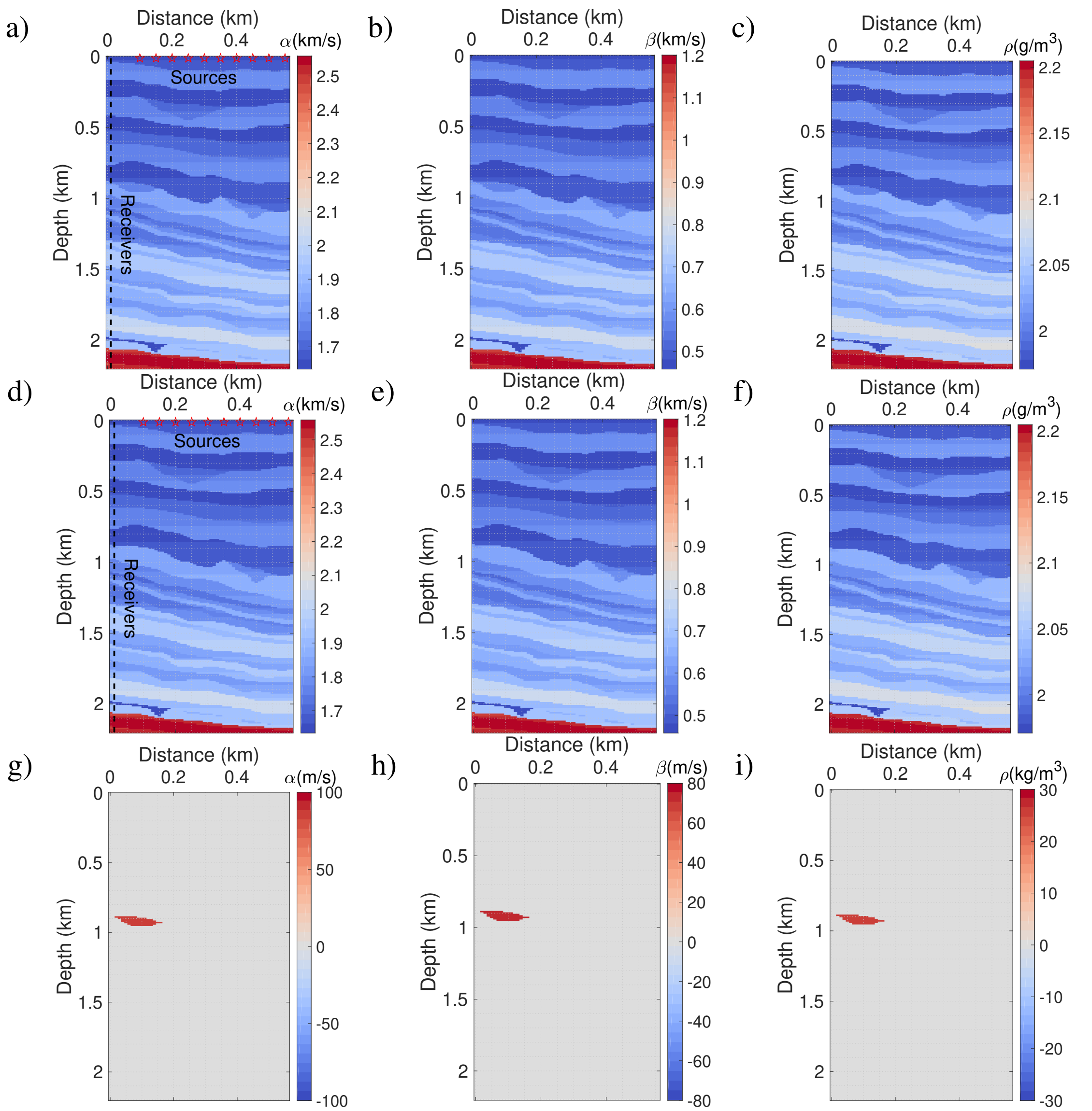

FIG. 2. True elastic models, the true baseline model includes the baseline P-wave velocity (a), the baseline S-wave velocity (b), and the baseline density (c), and the true monitor model includes the monitor P-wave velocity (d), the monitor S-wave velocity (e), and the monitor density (f). (g), (h), and (i) are the corresponding time-lapse changes (the monitor model minus the baseline model) of the three parameters, respectively. The acquisition geometries shown in (a) and (d) for baseline and monitor surveys, respectively, are identical. The red stars and dash lines represent sources and receiver locations, respectively.

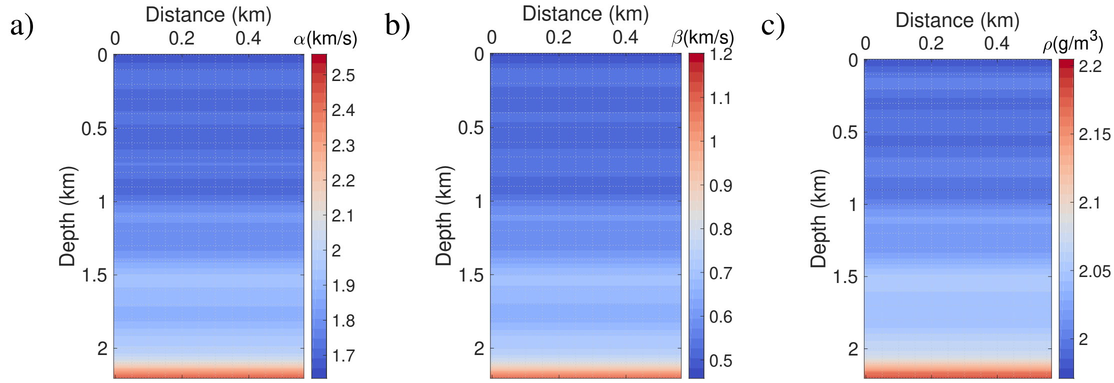

FIG. 3. Starting models that are identical for baseline and monitor inversion.

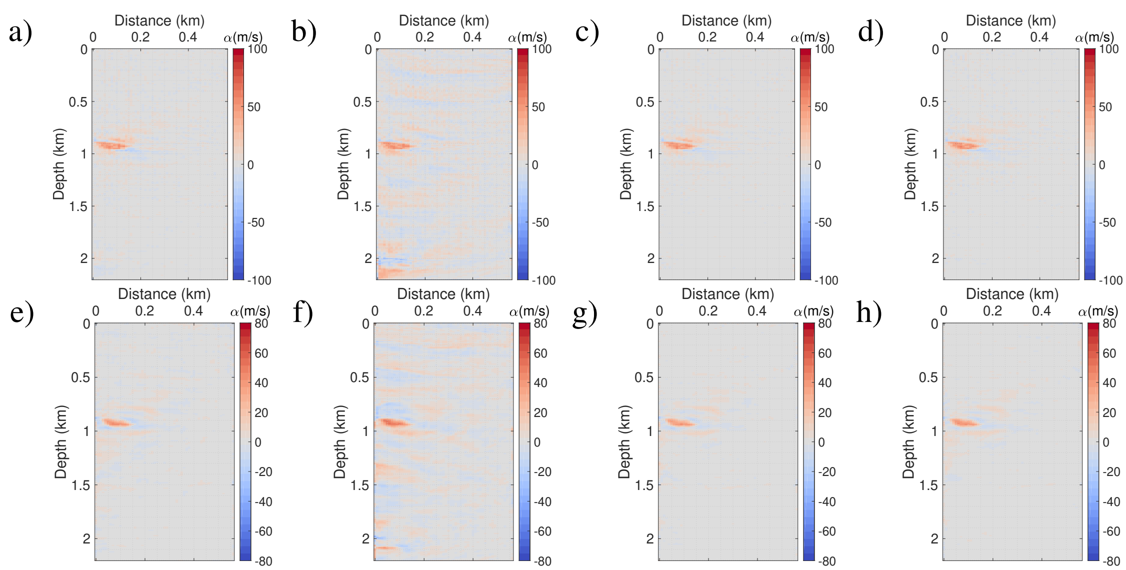

FIG. 4. Inverted results of time-lapse changes in the case that baseline and monitor surveys are perfectly repeated. The first row is the inverted P-wave velocity changes of the PRS (a), the SQS (b), the DDS (c), and the CMS (d). The second row is the inverted S-wave velocity changes of the PRS (e), the SQS (f), the DDS (g), and the CMS (h).

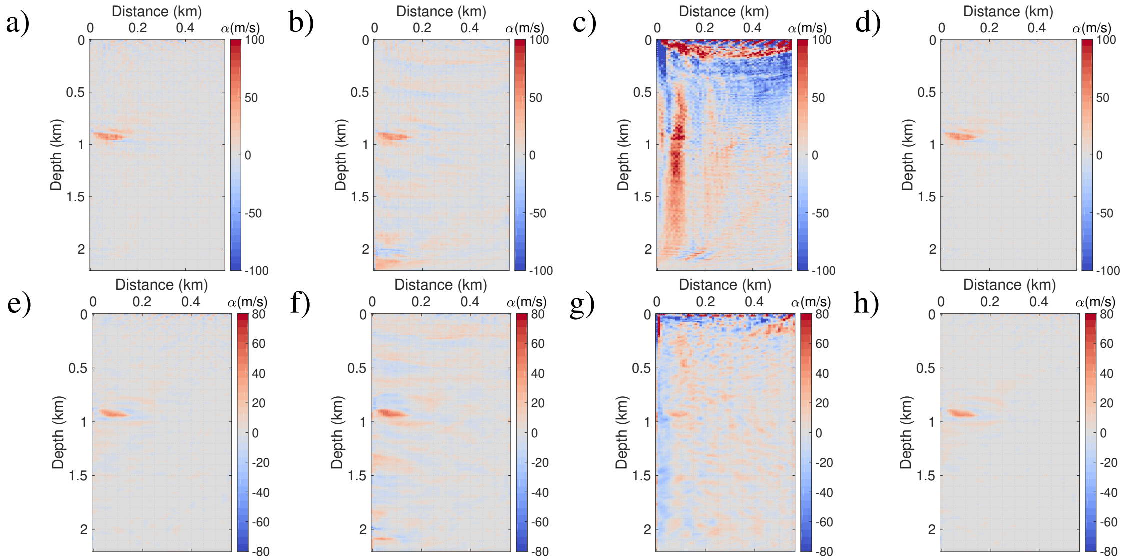

FIG. 5. Inverted results of time-lapse changes in the case that the source locations of the monitor survey are set 20 meters to the right of the baseline survey. The first row is the inverted P-wave velocity changes of the PRS (a), the SQS (b), the DDS (c), and the CMS (d). The second row is the inverted S-wave velocity changes of the PRS (e), the SQS (f), the DDS (g), and the CMS (h).

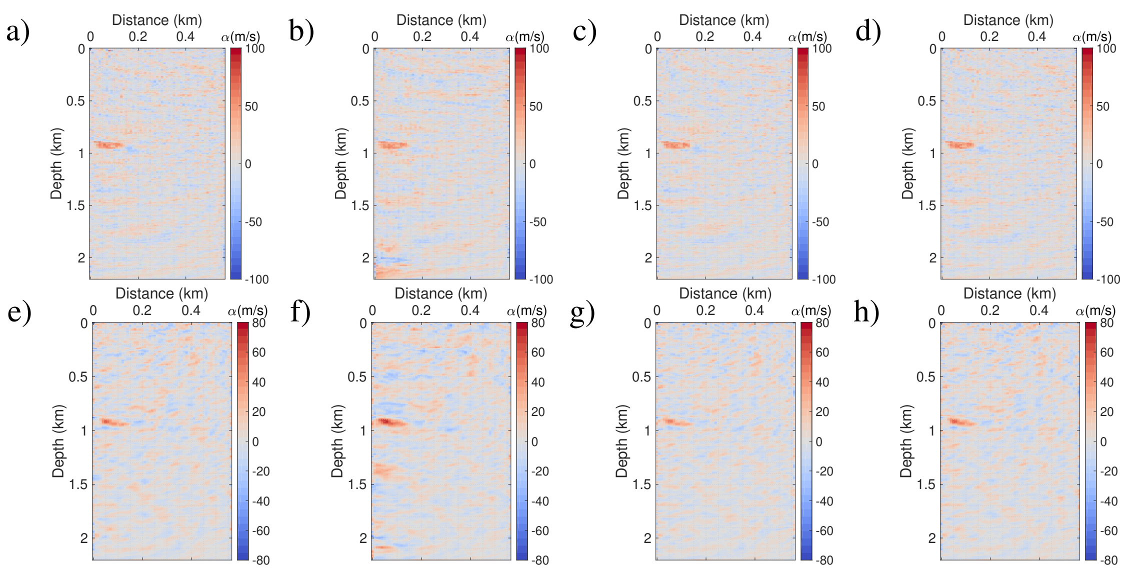

FIG. 6. Inverted results of time-lapse changes in the case that baseline and monitor surveys are perfectly repeated, but non-repeated random noises ($SNR = 20dB$) are added to baseline and monitor data, separately. The first row is the inverted P-wave velocity changes of the PRS (a), the SQS (b), the DDS (c), and the CMS (d). The second row is the inverted S-wave velocity changes of the PRS (e), the SQS (f), the DDS (g), and the CMS (h).

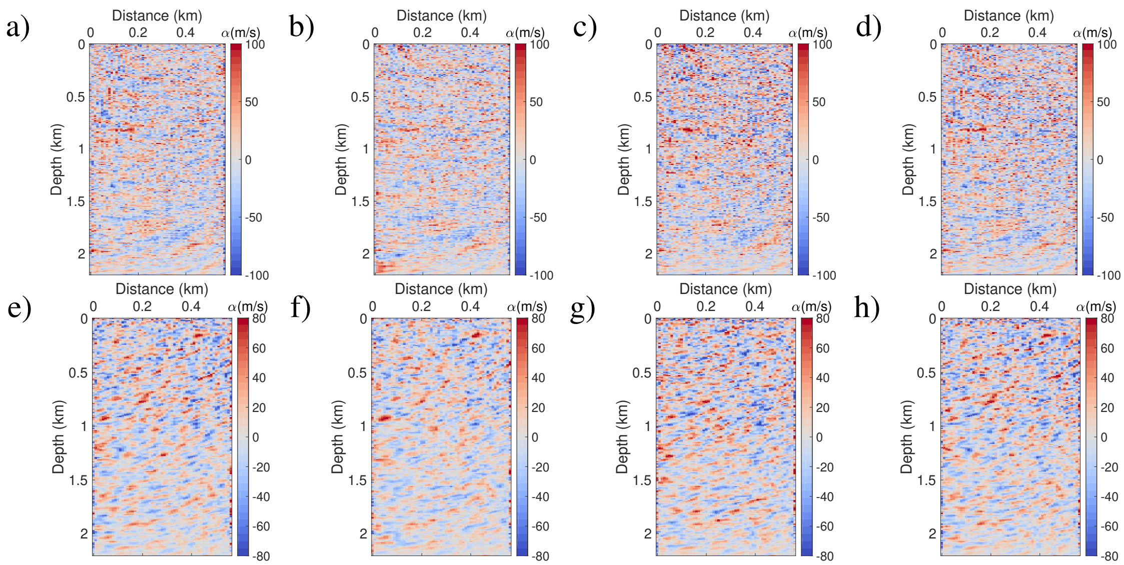

FIG. 7. Inverted results of time-lapse changes in the case that baseline and monitor surveys are perfectly repeated, but non-repeated random noises ($SNR = 10dB$) are added to baseline and monitor data, separately. The first row is the inverted P-wave velocity changes of the PRS (a), the SQS (b), the DDS (c), and the CMS (d). The second row is the inverted S-wave velocity changes of the PRS (e), the SQS (f), the DDS (g), and the CMS (h).

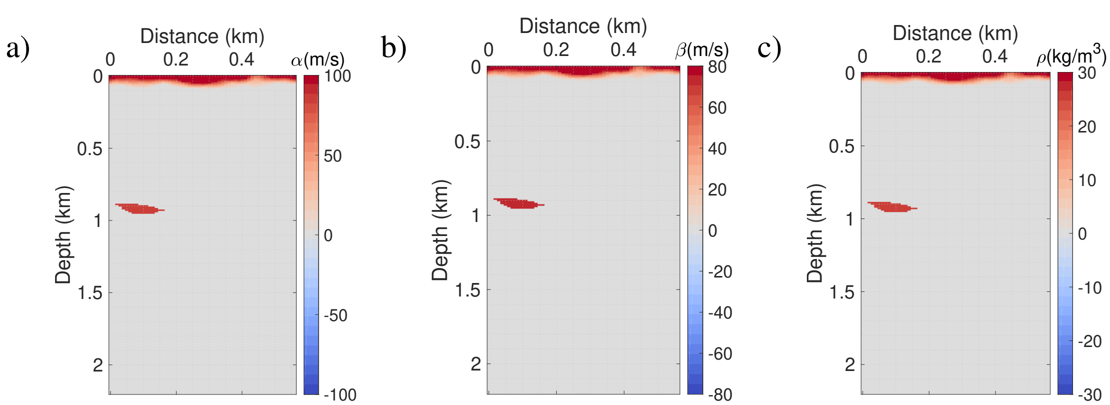

FIG. 8. (a), (b), and (c) are new time-lapse changes with near-surface property changes.

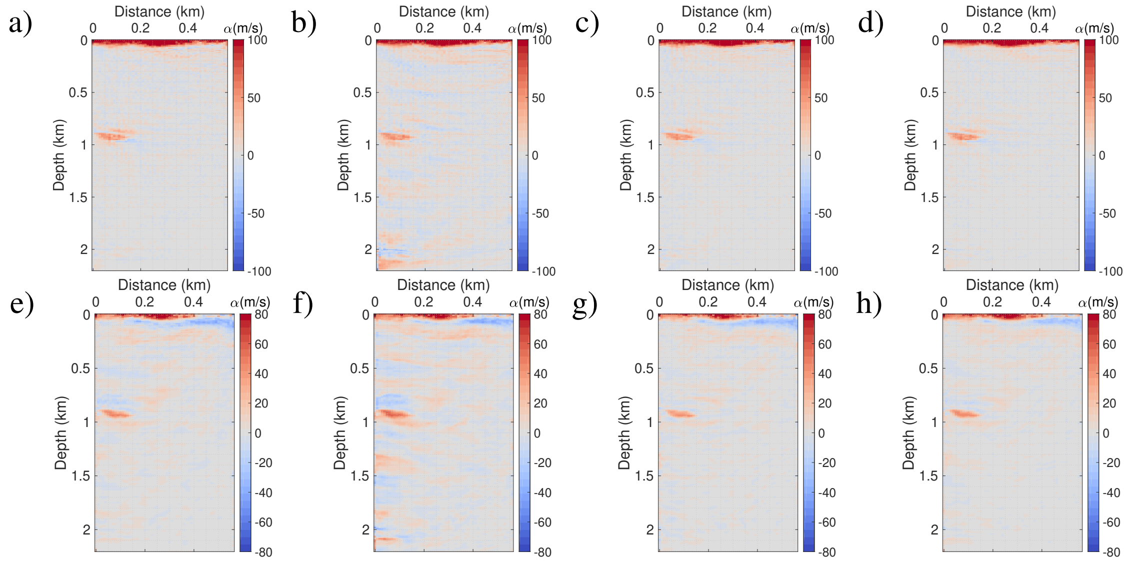

FIG. 9. Inverted results of the new time-lapse changes (Figure 8a-c) in the case that baseline and monitor surveys are perfectly repeated. The first row is the inverted P-wave velocity changes of the PRS (a), the SQS (b), the DDS (c), and the CMS (d). The second row is the inverted S-wave velocity changes of the PRS (e), the SQS (f), the DDS (g), and the CMS (h).

sources and receiver locations, respectively. Starting models that are identical for baseline and monitor inversion are plotted in Figure 3.

Inverted results of time-lapse changes for the four strategies (i.e., the PRS, the SQS, the DDS, and the CMS), in the case that baseline and monitor surveys are perfectly repeated, are plotted in Figure 4. Inverted results of time-lapse changes for the four strategies, in the case that the source locations of the monitor survey are set 20 meters to the right of the baseline survey, are plotted in Figure 5. Inverted results of time-lapse changes for the four strategies, in the case that baseline and monitor surveys are perfectly repeated, but non-repeated random noises ($SNR = 20dB$) are added to baseline and monitor data, separately, are plotted in Figure 6. Inverted results of time-lapse changes for the four strategies, in the case that baseline and monitor surveys are perfectly repeated, but non-repeated random noises ($SNR = 10dB$) are added to baseline and monitor data, separately, are plotted in Figure 7. In Figure 8, new time-lapse changes with near-surface property changes are plotted. And the corresponding results are plotted in Figure 9.

CONCLUSION

From the results in the above section, we can conclude: P-wave velocity changes can be better recovered than S-wave velocity changes; except for the DDS, the other three strategies have similar performance; the DDS also has similar performance to the others when acquisition geometries for baseline and monitor surveys are identical, but it is sensitive to the non-repeatability on source locations between twice surveys; no strategies can effectively handle the case of random noise; near-surface property changes have limit impact on the recovery of time-lapse changes for VSP data.

ACKNOWLEDGEMENTS

We thank the sponsors of CREWES for continued support. This work was funded by CREWES industrial sponsors, NSERC (Natural Science and Engineering Research Council of Canada) through the grants CRDPJ 543578-19. Partial funding also came from the Canada First Research Excellence Fund.

REFERENCES

Ajo-Franklin, J., Peterson, J., Doetsch, J., and Daley, T., 2013, High-resolution characterization of a co2 plume using crosswell seismic tomography: Cranfield, ms, usa: International Journal of Greenhouse Gas Control, **18**, 497–509.

Asnaashari, A., Brossier, R., Garambois, S., Audebert, F., Thore, P., and Virieux, J., 2015, Time-lapse seismic imaging using regularized full-waveform inversion with a prior model: which strategy?: Geophysical prospecting, **63**, No. 1, 78–98.

Bortoni, S., Barragan, S., Azevedo, G., Cypriano, L., Ferreira, A., Moreira, W., dos Reis, P., and Filho, W., 2021, Learnings from an fwi imaging study using 3d and 4d data over a postsalt field in campos basin, *in* First International Meeting for Applied Geoscience & Energy, Society of Exploration Geophysicists, 587–591.

Brossier, R., Operto, S., and Virieux, J., 2009, Robust elastic frequency-domain full-waveform inversion using the l1 norm: Geophysical Research Letters, **36**, No. 20.

Byerley, G., Monk, D., Aaron, P., and Yates, M., 2018, Time-lapse seismic monitoring of individual hydraulic frac stages using a downhole das array: The Leading Edge, **37**, No. 11, 802–810.

Calvert, R., 2005, Insights and methods for 4D reservoir monitoring and characterization: Society of Exploration Geophysicists and European Association of ....

Cheng, A., Huang, L., and Rutledge, J., 2010, Time-lapse vsp data processing for monitoring co 2 injection: The Leading Edge, **29**, No. 2, 196–199.

Cho, Y., and Jun, H., 2021, Estimation and uncertainty analysis of the co2 storage volume in the sleipner field via 4d reversible-jump markov-chain monte carlo: Journal of Petroleum Science and Engineering, **200**, 108,333.

Egorov, A., Pevzner, R., Bóna, A., Glubokovskikh, S., Puzyrev, V., Tertyshnikov, K., and Gurevich, B., 2017, Time-lapse full waveform inversion of vertical seismic profile data: Workflow and application to the co2crc otway project: Geophysical Research Letters, **44**, No. 14, 7211–7218.

Fu, X., and Innanen, K. A., 2021, An mcmc-based approach to time-lapse full-waveform inversion, *in* First International Meeting for Applied Geoscience & Energy, Society of Exploration Geophysicists, 3484–3489.

Fu, X., and Innanen, K. A., 2022a, Stepsize sharing in time-lapse full-waveform inversion, *in* Second International Meeting for Applied Geoscience & Energy, Society of Exploration Geophysicists, 473–477.

Fu, X., and Innanen, K. A., 2022b, A time-domain, multi-source bayesian/markov chain monte carlo formulation of time-lapse seismic waveform inversion: Geophysics, **87**, No. 4, 1–110.

Fu, X., and Innanen, K. A., 2022c, Time-lapse seismic imaging using shot gathers with non-repeatable source wavelets: Geophysics, **88**, No. 1, 1–108.

Fu, X., Romahn, S., and Innanen, K., 2020, Double-wavelet double-difference time-lapse waveform inversion, *in* SEG Technical Program Expanded Abstracts 2020, Society of Exploration Geophysicists, 3764–3767.

Greaves, R. J., and Fulp, T. J., 1987, Three-dimensional seismic monitoring of an enhanced oil recovery process: Geophysics, **52**, No. 9, 1175–1187.

Hicks, E., Hoeber, H., Houbiers, M., Lescoffit, S. P., Ratcliffe, A., and Vinje, V., 2016, Time-lapse full-waveform inversion as a reservoir-monitoring tool—a north sea case study: The Leading Edge, **35**, No. 10, 850–858.

Huang, X., Jakobsen, M., Eikrem, K. S., and Nævdal, G., 2018, A target-oriented scheme for efficient inversion of time-lapse seismic waveform data, *in* 2018 SEG International Exposition and Annual Meeting, OnePetro.

Jack, I., 2017, 4d seismic—past, present, and future: The Leading Edge, **36**, No. 5, 386–392.

Kotsi, M., Malcolm, A., and Ely, G., 2020, Uncertainty quantification in time-lapse seismic imaging: a full-waveform approach: Geophysical Journal International, **222**, No. 2, 1245–1263.

Lailly, P., Bednar, J. et al., 1983, The seismic inverse problem as a sequence of before stack migrations: Conference on Inverse Scattering, Theory and Application, Society for Industrial and Applied Mathematics, Expanded Abstracts, 206–220.

Landrø, M., 2001, Discrimination between pressure and fluid saturation changes from time-lapse seismic data: Geophysics, **66**, No. 3, 836–844.

Li, Y., Alkhalifah, T., and Guo, Q., 2021, Target-oriented time-lapse waveform inversion using deep learning-assisted regularization: Geophysics, **86**, No. 4, R485–R495.

Lumley, D., Adams, D. C., Meadows, M., Cole, S., and Wright, R., 2003, 4d seismic data processing issues and examples, *in* SEG Technical Program Expanded Abstracts 2003, Society of Exploration Geophysicists, 1394–1397.

Lumley, D. E., 2001, Time-lapse seismic reservoir monitoring: Geophysics, **66**, No. 1, 50–53.

Macquet, M., Lawton, D. C., Saeedfar, A., and Osadetz, K. G., 2019, A feasibility study for detection thresholds of co2 at shallow depths at the cami field research station, newell county, alberta, canada: Petroleum Geoscience, **25**, No. 4, 509–518.

Maharramov, M., Biondi, B. L., and Meadows, M. A., 2016, Time-lapse inverse theory with applicationstime-lapse inverse theory: Geophysics, **81**, No. 6, R485–R501.

Plessix, R.-E., Michelet, S., Rynja, H., Kuehl, H., Perkins, C., de Maag, J., and Hatchell, P., 2010, Some 3d applications of full waveform inversion, *in* 72nd EAGE Conference and Exhibition-Workshops and Fieldtrips, European Association of Geoscientists & Engineers, cp–162.

Pratt, R. G., 1990, Frequency-domain elastic wave modeling by finite differences; a tool for crosshole seismic imaging: Geophysics, **55**, No. 5, 626–632.

Raknes, E. B., and Arntsen, B., 2014, Time-lapse full-waveform inversion of limited-offset seismic data using a local migration regularization: Geophysics, **79**, No. 3, WA117–WA128.

Rickett, J., and Lumley, D., 2001, Cross-equalization data processing for time-lapse seismic reservoir monitoring: A case study from the gulf of mexico: Geophysics, **66**, No. 4, 1015–1025.

Routh, P., Palacharla, G., Chikichev, I., and Lazaratos, S., 2012, Full wavefield inversion of time-lapse data for improved imaging and reservoir characterization, *in* SEG Technical Program Expanded Abstracts 2012, Society of Exploration Geophysicists, 1–6.

Shulakova, V., Pevzner, R., Dupuis, J. C., Urosevic, M., Tertyshnikov, K., Lumley, D. E., and Gurevich, B., 2015, Burying receivers for improved time-lapse seismic repeatability: Co2crc otway field experiment: Geophysical Prospecting, **63**, No. 1, 55–69.

Tarantola, A., 1984, Inversion of seismic reflection data in the acoustic approximation: Geophysics, **49**, No. 8, 1259–1266.

Tarantola, A., 1986, A strategy for nonlinear elastic inversion of seismic reflection data: Geophysics, **51**, No. 10, 1893–1903.

Virieux, J., and Operto, S., 2009, An overview of full-waveform inversion in exploration geophysics: Geophysics, **74**, No. 6, WCC1–WCC26.

Willemsen, B., Cao, J., and Roy, B., 2016, The impact of the acoustic approximation on time-lapse fwi, *in* 2016 SEG International Exposition and Annual Meeting, OnePetro.

Willemsen, L. A., 2017, Problems with a localized nature in exploration seismology: Ph.D. thesis, Massachusetts Institute of Technology.

Wilson, G. A., Willis, M. E., and Ellmauthaler, A., 2021, Evaluating 3d and 4d das vsp image quality of subsea carbon storage: The Leading Edge, **40**, No. 4, 261–266.

Yang, D., Liu, F., Morton, S., Malcolm, A., and Fehler, M., 2016, Time-lapse full-waveform inversion with ocean-bottom-cable data: Application on valhall field: Geophysics, **81**, No. 4, R225–R235.

Yang, D., Meadows, M., Inderwiesen, P., Landa, J., Malcolm, A., and Fehler, M., 2015, Double-difference waveform inversion: Feasibility and robustness study with pressure data: Geophysics, **80**, No. 6, M129–M141.

Zhang, Z., and Huang, L., 2013, Double-difference elastic-waveform inversion with prior information for time-lapse monitoring: Geophysics, **78**, No. 6, R259–R273.

Zheng, Y., Barton, P., and Singh, S., 2011, Strategies for elastic full waveform inversion of time-lapse ocean bottom cable (obc) seismic data, *in* SEG Technical Program Expanded Abstracts 2011, Society of Exploration Geophysicists, 4195–4200.

Zhou, W., and Lumley, D., 2021a, Central-difference time-lapse 4d seismic full-waveform inversion: Geophysics, **86**, No. 2, R161–R172.

Zhou, W., and Lumley, D., 2021b, Nonrepeatability effects on time-lapse 4d seismic full-waveform inversion for ocean-bottom node data: Geophysics, **86**, No. 4, R547–R561.

Zwartjes, P., Mateeva, A., Chalenski, D., Duan, Y., Kiyashchenko, D., and Lopez, J., 2018, Frequent, multi-well, stand-alone 3d das vsp for low-cost reservoir monitoring in deepwater, *in* SEG Technical Program Expanded Abstracts 2018, Society of Exploration Geophysicists, 4948–4952.